Chaos, Solitons and Fractals 181 (2024) 114601

Contents lists available at ScienceDirect

Chaos, Solitons and Fractals

journal homepage: www.elsevier.com/locate/chaos

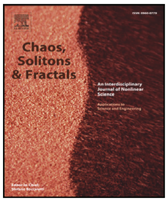

Electromechanical memcapacitor model offering biologically plausible spiking

Zixi Zhang [a], Yuriy V. Pershin [b,*], Ivar Martin [c]

[a] School of Physics, Peking University, Beijing, 100871, China
[b] Department of Physics and Astronomy, University of South Carolina, Columbia, SC, 29208, USA
[c] Materials Science Division, Argonne National Laboratory, Argonne, IL, 08540, USA

ARTICLE INFO

Keywords:
Memcapacitor
Neuron
Artificial neural networks
Spiking neurons
Nonlinear dynamics
Memristor

ABSTRACT

In this article, we introduce a new nanoscale electromechanical device – a leaky memcapacitor – and show that it may be useful for the hardware implementation of spiking neurons. The leaky memcapacitor is a movable-plate capacitor that becomes quite conductive when the plates come close to each other. The equivalent circuit of the leaky memcapacitor involves a memcapacitive and memristive system connected in parallel. In the leaky memcapacitor, resistance and capacitance depend on the same internal state variable, which is the displacement of the movable plate. We have performed a comprehensive analysis showing that several types of spiking observed in biological neurons can be implemented with the leaky memcapacitor. Significant attention is paid to the dynamic properties of the model. As in leaky memcapacitors the capacitive, leaking resistive, and reset functionalities are implemented naturally within the same device structure, their use will simplify the creation of spiking neural networks.

1. Introduction

Information processing in biological systems is based on a complex network of interacting neurons. Each neuron, when subjected to a stimulus, responds by outputting a signal that typically has a form of unharmonic spikes. A variety of models of the spiking phenomenon have been proposed, most famously the Hodgkin–Huxley (HH) model, which successfully captured many observed features of spiking in neuronal membranes [1–7]. This model led to the development of biochemically based information processing models in subsequent decades [6,8–10].

HH model attempts to accurately capture the properties of ion channels with memory and, consequently, is quite complex. Several simplified models, such as the integrate-and-fire model, appeared that can achieve a variety of spiking behaviors in response to different types of stimulation [6,7,11–15]. Although distinct from HH, one may expect that qualitative features such as instabilities/bifurcations, limit cycles, and synchronization among neurons are quite universal and robust due to the general underlying principles of dynamical systems [16]. However, simplified models may have the important advantage of being easier to implement artificially using existing materials and devices [17]. This leads to the exciting possibility of biologically inspired *neuromorphic* information processing systems implemented in the solid state.

In the above context, the class of memory circuit elements [18] becomes increasingly important because of the capacity of memory circuit elements to store and process information on the same physical platform [19]. The memory circuit elements (in a pure form) are resistors, capacitors, and inductors with memory whose response is defined by the equations

$$y(t) = g(\mathbf{x},u)\,u(t) \ , \tag{1}$$

$$\dot{\mathbf{x}} = \mathbf{f}(\mathbf{x},u) \ , \tag{2}$$

where $y(t)$ and $u(t)$ are any two complementary circuit variables (i.e., current, charge, voltage, or flux), $g(\mathbf{x},u)$ is a generalized response, $\mathbf{x}$ is a set of n state variables describing the internal state of the device, and $\mathbf{f}(\mathbf{x},u)$ is a continuous n-dimensional vector function. Depending on the choice of the complementary circuit variables, Eqs. (1) and (2) are used to define memristive, memcapacitive, or meminductive systems [18]. Examples of physical realizations of memory circuit elements can be found in the review paper [20].

For more than a decade, significant attention has been paid to the application of memristive systems in neuromorphic computing. Indeed, memristive systems share several common characteristics with biological synapses, such as the two-terminal structure, adaptivity, and high integration density. One of the first works in this area was

---

* Corresponding author.
E-mail addresses: zixizhang@pku.edu.cn (Z. Zhang), pershin@physics.sc.edu (Y.V. Pershin), ivar@anl.gov (I. Martin).

https://doi.org/10.1016/j.chaos.2024.114601
Received 21 October 2023; Received in revised form 23 January 2024; Accepted 10 February 2024

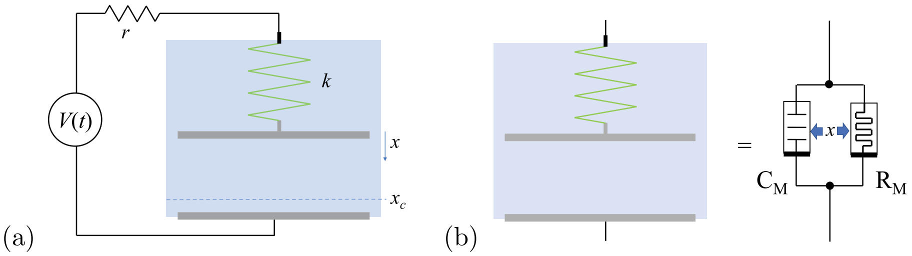

Fig. 1. (a) An electromechanical leaky memcapacitor connected to a voltage source through a resistor. (b) Equivalent electronic circuit of the leaky memcapacitor: a memcapacitive system, C_M, and a memristive system, R_M, connected in parallel. Both systems depend on the same state variable x.

the demonstration of associative memory with memristive neural networks by one of us [21]. Interestingly, the relevance of the memristive equations to the HH model was established in 1976 by Chua and Kang [22,23]. According to these authors, "the potassium channel of the Hodgkin–Huxley model should be identified as a first-order time-invariant voltage-controlled memristive one-port and the sodium channel should be identified as a second-order time-invariant voltage-controlled memristive one-port" [22]. Typically, the capacitive component in the response of memristive cells [24–28] is considered parasitic. Although most of the existing research focuses on purely electronic schemes, there are also models that rely on the mechanical realization of memory and spikes [24–28].

Neuromorphic applications of memcapacitive systems have received much less attention. This may be explained by the fact that in general memcapacitive devices [29–32] have been much less studied (compared to memristive ones). At the same time, the reactive nature of the capacitive response is very promising for low-power computing applications as, at equilibrium, the memcapacitive devices do not consume any power. Therefore, currently, the application of memcapacitors in neuromorphic circuits [33,34] is a narrow but highly promising research field. In fact, the possibility of energy-efficient neuromorphic computing with solid-state memcapacitive structures has been recently demonstrated [35].

The mechanical aspect of biological neurons is also becoming increasingly recognized as important in the study of neuroscience. It plays a role in several physiological processes, including the generation of action potentials [36]. Mechanical changes in the cell membrane can influence the opening and closing of ion channels, which can affect the electrical signaling of the neuron. The soliton model combines mechanical and electrical factors of signal propagation through axons and has been able to account for some experimental effects in anesthesiology beyond the Hodgkin–Huxley model [37–40].

In this work, in part inspired by biological neurons, we propose a simple neuromorphic electromechanical model based on a leaky memcapacitor. The proposed model can be used to generate periodic spike timing sequences under constant stimulation. As the operation of the leaky memcapacitor is based on the mechanical degree of freedom, its behavior is pretty unique and different from that of memristive ReRAM cells. Applying the methods of dynamical systems, we explore the qualitative features of this model in terms of its fixed points, bifurcations, and limit cycles under DC stimulation. In addition, we demonstrate that the system is capable of complex dynamical adaptations, such as synchronization with periodic external drives, spiking frequency drift, bursting, and other adaptations (for some behaviors, an additional memory circuit element is required).

2. The model

In this section, we introduce a leaky memcapacitor, its model, and the circuit we use to simulate the spiking neurons. The circuit, the physical diagram of the leaky memcapacitor, and its equivalent circuit are shown in Fig. 1.

The central element of our spiking neuron is a *leaky memcapacitor* – a capacitor with a plate that moves in response to the force exerted by the internal electric field and the restoring force of the spring (the spring constant is k). In the absence of charges on the plates, $q = 0$, the distance between two plates is d. It is assumed that the displacement of the top plate, x, is positive for the displacement towards the bottom plate, see Fig. 1(a). Thus, the distance between the plates is $d - x$. The response of this capacitor to the change in voltage takes a finite time as physically the response cannot be instantaneous. Consider a fully discharged leaky memcapacitor subjected to a small step-like voltage. It is evident that right after the step, the displacement of its top plate remains the same as the initial one (zero), and only after a finite time the top plate will approach a new equilibrium position. Such memory of the prior state, of course, is volatile. Below, we explicitly show that the model of the capacitive component of the system in Fig. 1(b) (left) belongs to the class of memcapacitive systems [18].

We assume that the capacitor is *leaky*: there is a finite resistance $R(x)$, which depends on the distance between the plates, rapidly dropping in the 'contact' region, $x > x_c$. The leaky memcapacitor has *memory* (which justifies the term memcapacitor) because the current position of the moving plate (and hence the capacitance itself) depends on the prior history of the charge on the capacitor, which in turn depends on the history of applied voltage. It is this history dependence, the memory, that is responsible for the emergence of complex behaviors that the simple circuit in Fig. 1(a) exhibits.

The main operating principle of this device is straightforward. Starting from the equilibrium position at $x = 0$, upon turning on the voltage V, the capacitor begins to charge up. This leads to the attraction between its plates, which brings them closer together. For a sufficiently large applied voltage, the top plate reaches the contact region, the capacitor discharges, and the plate recoils back from the contact region. Note that the charging process is limited by the resistor with resistance r (Fig. 1(a)).

We found that the proximity-induced attraction between the two surfaces (plates) is helpful to prevent the plates from finding a new static equilibrium position in the contact region. We model this part of the interaction with a Lennard-Jones-like potential. The short-range attraction between the plates allows for a more effective discharge process, leading to a periodic approach of the top plate to the bottom plate followed by recoil. The exact form of $R(x)$ and the form of the potential do not matter, to a certain extent. In the biological context, our memcapacitor may represent two lipid monolayers forming a cell membrane. As the membrane swells or thins, the resistance of the membrane (through ion channels) is affected, as modeled by $R(x)$.

In our modeling of membrane dynamics, we neglect the kinematic mass (in a biological setting, that would be because membranes reside in an aqueous environment that has considerable viscosity). This overdamped regime makes it non-trivial to have oscillatory behavior, and new types of mechanism are required to perform the periodic spiking that we see possible.

Eqs. (1) and (2) provide the general framework for the description of leaky memcapacitor. For the capacitive and resistive responses, Eq. (1) is written as

$$q = \frac{\epsilon A}{d - x} V_C \equiv C(x) \cdot V_C, \tag{3}$$

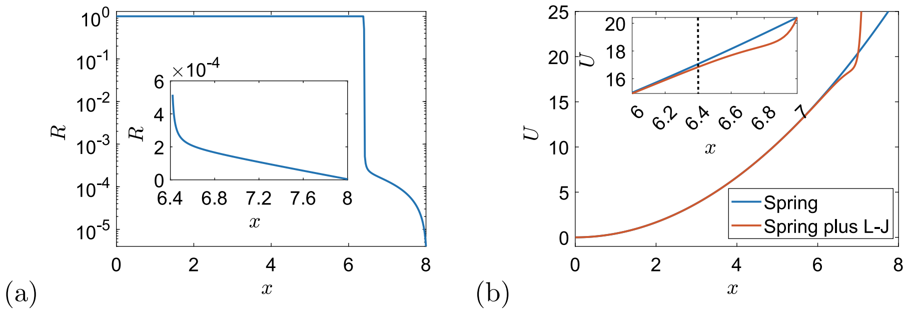

Fig. 2. (a) Resistance as a function of the displacement of the top plate (Eq. (4)). (b) Potential energy as a function of the displacement of the top membrane (Eq. (6)). The insets show a zoomed-in contact region. The dashed line refers to x_c.

Table 1
Parameters used in simulations. Some of the parameters are not shown, as they play the role of units of measure (e.g. R_0).

Parameter	Value	Parameter	Value
d	8	r	10^{-3}
x_c	6.4	ρ_0	1.25×10^{-4}
β	5×10^4	γ	1.25×10^{-4}
k	5/6		

$$V_C = \left[R_0 \cdot \left(\frac{1}{\pi}\arctan\beta\left(x_c - x\right) + 0.5\right) + \rho_0 \frac{d-x}{A}\right] I_M \equiv R(x) \cdot I_M, \tag{4}$$

where q is the memcapacitor charge, V_C is the voltage across the leaky memcapacitor, I_M is the leakage current, ϵ is the permittivity, A is the plate area, and R_0, β, ρ_0 are the parameters defining the memristance. In the normal regime, $R(x) \approx R_0$, while in the contact regime, $R(x)$ is mainly determined by the ρ_0 term; β describes the rate of change of the R_0 component in $R(x)$ in the vicinity of x_c.

The leaky memcapacitor is described by a single internal state variable x, which is the displacement of the top plate from its equilibrium position (at $q = 0$) in the downward direction (see Fig. 1(a)). Its dynamics (corresponding to Eq. (2)) is represented by

$$\gamma \dot{x} = \frac{q^2}{\epsilon A} - \frac{\mathrm{d}U(x)}{\mathrm{d}x} \quad , \tag{5}$$

where γ is the dissipation coefficient, and the potential $U(x)$ is chosen as

$$U(x) = \frac{1}{2}kx^2 + 4\epsilon_l \left[\left(\frac{\sigma}{d-x}\right)^{12} - \left(\frac{\sigma}{d-x}\right)^{6}\right] \quad . \tag{6}$$

Here, the first term is the spring potential energy, while the second term is the Lennard-Jones-like potential that we use to describe the contact interaction between the plates. In Eq. (6), k is the spring constant, ϵ_l is the depth of the Lennard-Jones potential well, and σ is the distance at which the Lennard-Jones potential energy is zero.

In the following, we measure the distances in units of σ, resistances in R_0, U in ϵ_l, k in ϵ_l/σ^2, time in $R_0 A\epsilon/\sigma$, charge in $\sqrt{\epsilon\epsilon_l A/\sigma}$, γ in $\epsilon\epsilon_l A R_0/\sigma^3$, voltage in $\sqrt{\sigma\epsilon_l/(\epsilon A)}$, and current in $\sqrt{\sigma\epsilon_l/\epsilon A}/R_0$. To minimize clutter in the text, the original notation is used for dimensionless variables and parameters. The parameters used in our simulations are given in Table 1. Fig. 2(a) shows $R(x)$ as defined by Eq. (4); Eq. (6) is presented in Fig. 2(b).

Note that qualitatively similar results (to the ones presented in this paper) may be obtained using a different choice of parameters and functional dependencies. In particular, we have verified that the results remain nearly the same when the constant resistance for $x \lesssim 6$ in Fig. 2(a) is replaced with a resistance linearly dependent on x (for more details, see Supplemental Information (SI) Sec. S1).

To simulate Fig. 1(a) circuit, we use Kirchhoff's voltage law

$$V(t) = r\left(\dot{q} + I_M\right) + V_C \quad , \tag{7}$$

which is applied together with the equations defining the leaky memcapacitor, Eqs. (3)–(6). Trajectories $(x(t), q(t))$ are found by numerical integration of Eqs. (5) and (7). Integration was performed using the ODE solver ode45 for non-stiff differential equations in MATLAB® ver. R2022a.

For the convenience of the reader, Eqs. (5) and (7) can be presented as

$$\dot{x} = \frac{q^2}{\gamma\epsilon A} - \frac{kx}{\gamma} - \frac{24\epsilon_l}{\gamma}\left[\frac{2\sigma^{12}}{(d-x)^{13}} - \frac{\sigma^6}{(d-x)^7}\right] \quad , \tag{8}$$

$$\dot{q} = \frac{V(t)}{r} - q\frac{d-x}{\epsilon A}\left[\frac{1}{r} + \frac{1}{R_0\left(\frac{1}{\pi}\arctan\beta\left(x_c - x\right) + 0.5\right) + \rho_0\frac{d-x}{A}}\right]. \tag{9}$$

We note that our model of spiking neurons (Eqs. (8) and (9)) is distinct from all other spiking models (see, e.g., [6,17]).

3. Spiking behavior and phase diagram

Figs. 3(a) and (b) show two selected simulation results that demonstrate the transient dynamics from zero initial conditions, $x_0 = 0$ and $q_0 = 0$, to the regime of periodic spiking. These results indicate a significant dependence of the shape of the spike on the magnitude of the applied voltage ($V = 8.0829$ in Fig. 3(a) and $V = 15.0111$ in Fig. 3(b)). According to Figs. 3(a) and (b), the spikes are smoother at $V = 8.0829$, and sharper at $V = 15.0111$. The sharper spikes show a closer qualitative resemblance to biological spikes.

A notable feature of the transient dynamics is the initial sharp increase in the voltage across the leaky memcapacitor, V_C. This property (clearly observed in Figs. 3(a) and (b)) is associated with the smaller capacitance at short times (close to $t = 0$) due to the initially large plate separation. Within the transient region, the leaky memcapacitor adapts to the applied voltage: the Coulomb attraction reduces the distance between the plates, which increases the capacitance. The voltage plateau in Fig. 3(a) is close to the bifurcation point at $V_1' = 7.9582$ (for more information, see SI Sec. S1). This explains the relatively long duration of the transient region.

Moreover, in Fig. 3(c) we present an example of nonspiking behavior. In this case, the trajectory ends in a sink (attractor).

We systematically analyzed the behavior of the circuit by studying its fixed points and limit cycles. For this purpose, we used vector field diagrams of solutions and Jacobi matrices (for more information, see SI Sec. S1). This analysis resulted in the phase diagram presented in Fig. 4(a). The diagram indicates the presence of a global limit cycle in a wide range of applied voltage, from V_1' to V_2, which accounts for the presence of the spiking regime.

The main features of the phase diagram are as follows. First, since the behavior is symmetric with respect to the sign of V, we show only the positive voltage region of the phase diagram. Around $V = 0$, the only global attractor is a sink. As V increases, at $V_0 \approx 3.4156$ there is a bifurcation that nucleates a saddle and a spiral source; they do not influence the global attractor, however, until they separate sufficiently at V_1 where the saddle divides the phase space into two disconnected

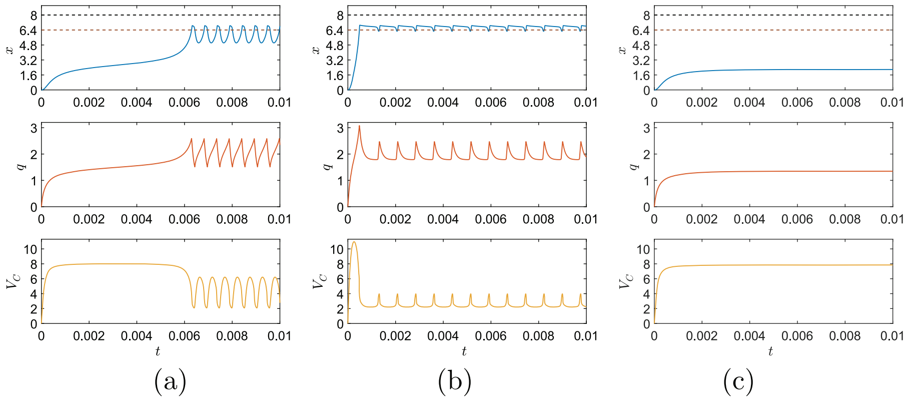

Fig. 3. Response to a step-like voltage applied at $t = 0$: starting from zero initial conditions ($x = 0$, $q = 0$), the circuit transits to (a), (b) a periodic spiking regime, or (c) a static regime. These graphs were obtained using (a) $V = 8.0829$, (b) $V = 15.0111$, and (c) $V = 7.8520$. In the top panels, the black dashed line refers to d and the brown one refers to x_c. (For interpretation of the references to color in this figure legend, the reader is referred to the web version of this article.)

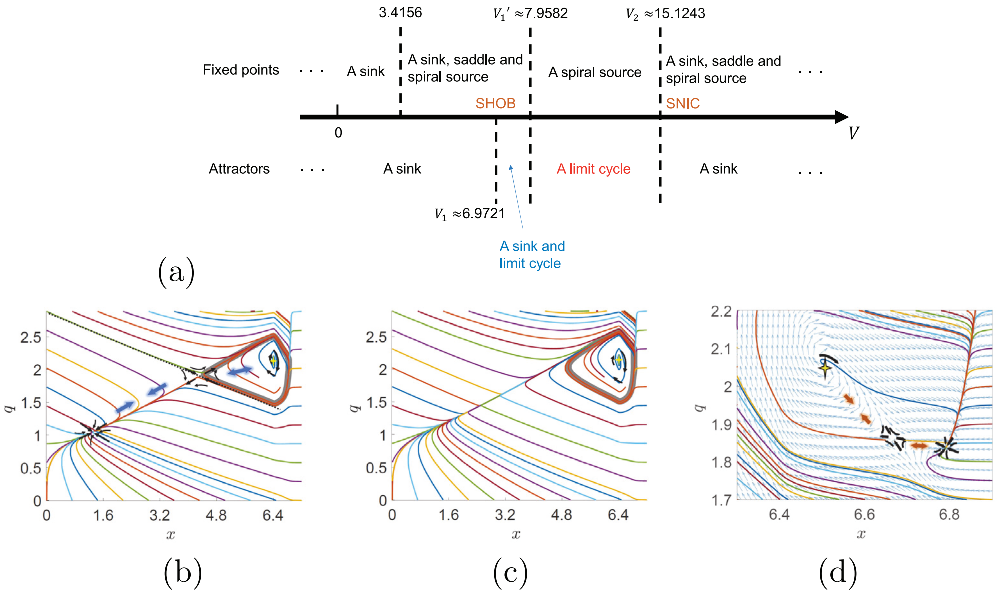

Fig. 4. (a) Fixed points and attractors as a function of the applied voltage V. Phase diagrams in (b) $V = 7.0437$ (the sink and limit cycle case in (a)), (c) $V = 7.9674$ (the limit cycle case in (a)) and (d) $V = 15.5000$ (the sink case on the right of the limit cycle one in (a)). In (b), the phase space is divided into two parts by the flow lines towards the saddle, as depicted with a dashed line. The semi-transparent gray thick line represents the limit cycle. The saddle, the sink, and the spiral source are labeled with black arrows, and the yellow star inside the limit cycle is located at the spiral source. The blue arrows in (b) and the orange arrows in (d) depict the direction of the shift of the three fixed points as V increases. In (d), the vector fields are added in small blue arrows to help show the fixed points. The initial conditions of the solutions are set discretely along the edge as well as around the spiral source. In (b)–(d), the evolution time t was 0.05. (For interpretation of the references to color in this figure legend, the reader is referred to the web version of this article.)

regions (saddle homoclinic orbit bifurcation (SHOB)), one of which hosts a limit cycle and the other the original sink that corresponds to a static state, as shown in Fig. 4(b). In SI Sec. S2 we show the possibility of switching between these two attractors using voltage pulses. Another bifurcation (saddle–node bifurcation) occurs when the sink and saddle points annihilate at $V_1' = 7.9582$, transforming the limit cycle into a global attractor with stable spikes, as shown in Fig. 4(c). At V_2, another bifurcation generating a sink-saddle pair cuts off the limit cycle, shifting the global attractor to the sink (saddle–node on the invariant circle (SNIC)), as shown in Fig. 4(d). As V continues to increase, the saddle and spiral source point move toward each other and then annihilate through a saddle–node bifurcation, leaving only a sink (for more information, see SI Sec. S1).

To better understand the properties of the spikes, the *natural* frequency of the spikes, $w_{natural}$, was calculated as a function of the applied voltage (see Fig. 5(a)). Interestingly, the calculated points are distributed in the half-of-the-oval shape in the frequency-voltage plot. Fig. 5(a) shows that the frequency approaches zero when $V \to V_1, V_2$. The Fourier transform of the voltage across the memcapacitor is presented in Fig. 5(b). Qualitatively, the entire spiking regime can be divided into three parts, I, II, and III, which are different by the pattern of spikes (see Figs. 5(c)–(e)). The regime of “negative spikes” I, and the regime of “positive spikes”, III, are connected by the regime of more symmetric (harmonic) spikes, II.

4. Synchronization with external source

To study synchronization with an external source, an ac voltage was added to the constant driving voltage V_{dc}, $V(t) = V_{dc} + \delta V \sin(\omega_{source} t)$, with $\delta V = 0.1155$. To initialize the system close to the limit cycle, we used the initial conditions $x_0 = 6.60$ and $q_0 = 2.02$. The Fourier transforms for the regimes I-III of oscillations in Fig. 5(a) are presented in Fig. 6. When the circuit is in regime II (Fig. 6(b)), i.e., away from the thresholds, the synchronization occurs only when the source

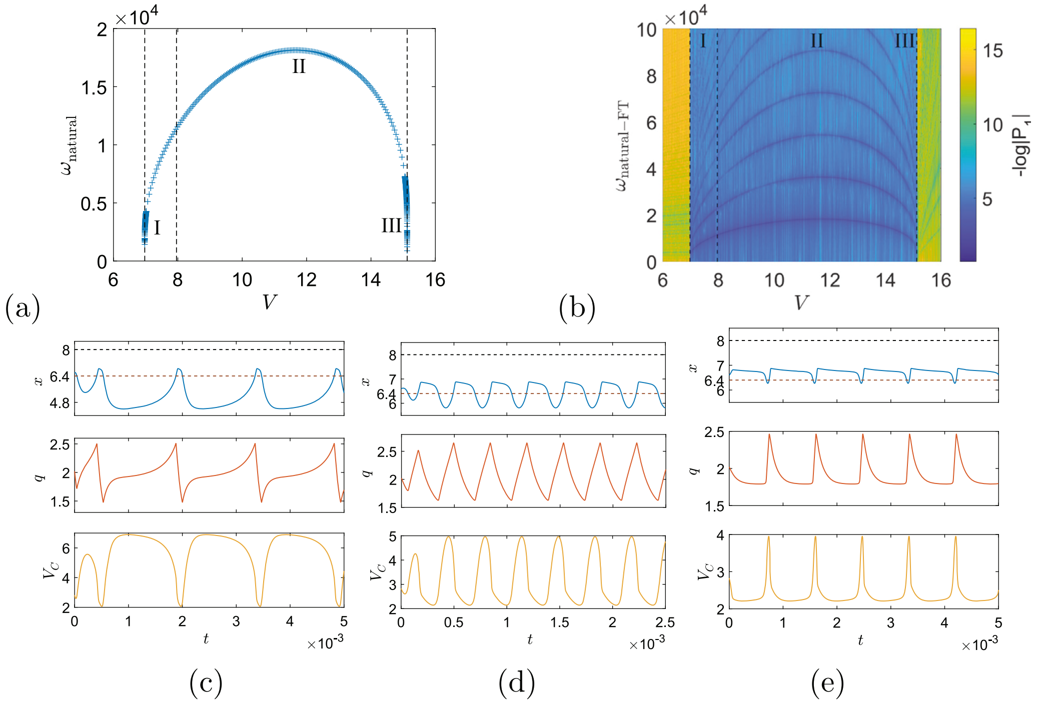

Fig. 5. (a) Spike frequency as a function of V, and (b) Fourier transform of V_C as a function of V. The dashed lines, from left to right, refer to V_1, V_1' and V_2, respectively. Here, P_1 is the single-sided amplitude of the Fourier transform. In these calculations, to keep the system close to the limit cycle, the initial condition was selected as $x_0 = 6.6000$ and $q_0 = 2.0207$. The evolution time t was 1.5, and we skipped the initial transient interval. (c)–(e) Steady-state oscillations at (c) $V = 7.0183$ (regime I), (d) $V = 11.5470$ (regime II) and (e) $V = 15.0561$ (regime III). In (c)–(e), the black dashed line refers to d and the brown line refers to x_c. (For interpretation of the references to color in this figure legend, the reader is referred to the web version of this article.)

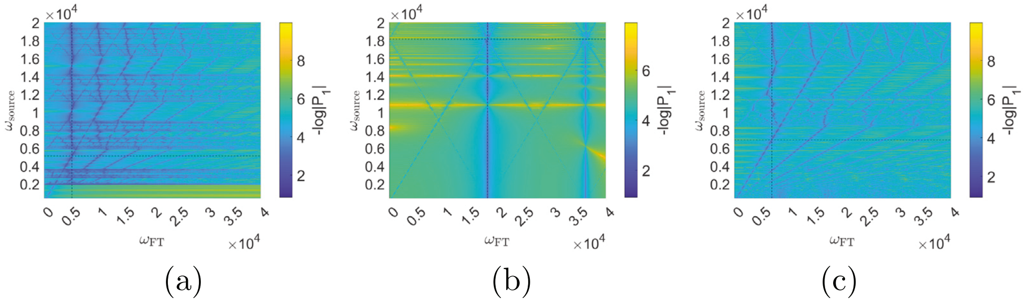

Fig. 6. Synchronization with external source: The Fourier transform of V_C for (a) $V_{dc} = 7.0645$ (regime I), (b) $V_{dc} = 11.5470$ (regime II) and (c) $V_{dc} = 15.0688$ (regime III). P_1 is the single-sided amplitude of the Fourier transform. In these calculations, to keep the system close to the limit cycle, the initial condition was selected as $x_0 = 6.6000$ and $q_0 = 2.0207$. These plots were obtained using the integration time t of 2; the initial interval of transient dynamics was omitted. In (a)–(c), the horizontal and vertical dashed lines correspond to $\omega_{natural}(V_{dc})$.

frequency is very close to the spike frequency, $\omega_{source} \approx \omega_{natural}(V_{dc})$. In this regime, the Fourier plot features various combinations of integer multiples of ω_{source} and $\omega_{natural}$, $N\omega_{natural} \pm M\omega_{source}$, where $M, N = 0, 1, 2, \ldots$

In the other two cases in Fig. 6, the external source has a much stronger influence on spike generation. Figs. 6(a) and (c) represent the cases when V_{dc} is close to the thresholds V_1 and V_2. In these cases, the regions of synchronized driving frequencies are largely extended in both integer multiples and rational fractions of the self-oscillation frequencies. In regime I, when the driving frequency is small, the system responds harmonically to the drive, as shown in Fig. 6(a), where only the component of ω_{source} is evident. This is because once V drops below V_1, the spiral source and saddle vanish simultaneously, and the system can easily switch to the sink, which is away from the contact regime as depicted in Figs. 4(a) and (b), and may not return. On the contrary, in regime III, when V crosses over V_2, the bifurcation of a sink-saddle pair SNIC bifurcation appears in the contact regime on the previous limit cycle, as depicted in Figs. 4(a) and (d), thus the system will not go away from the contact regime, resulting in a spiking waveform even at low source frequency. Fourier transforms for these three regimes are provided in SI Sec. S3.

5. Other types of dynamics

In this section, we show that the dynamics of Fig. 1(a) circuit can be further enriched by the use of additional components with memory. Specifically, we demonstrate that the replacement of the resistor r in Fig. 1(a) with a thermistor (a type of memristor [20,22]) may qualitatively change the pattern of spikes in several ways. Five types of modified behavior have been identified including bursting (a pattern of firing wherein the periods of rapid spiking are separated by quiescent periods).

In principle, it is evident that at a suitable constant applied voltage V, the resistance r controls the generation of spikes. As in the limiting cases of $r \to 0$ and $r \to \infty$ the dynamics of Fig. 1(a) circuit should not be oscillatory, one can assume that the spiking behavior occurs within

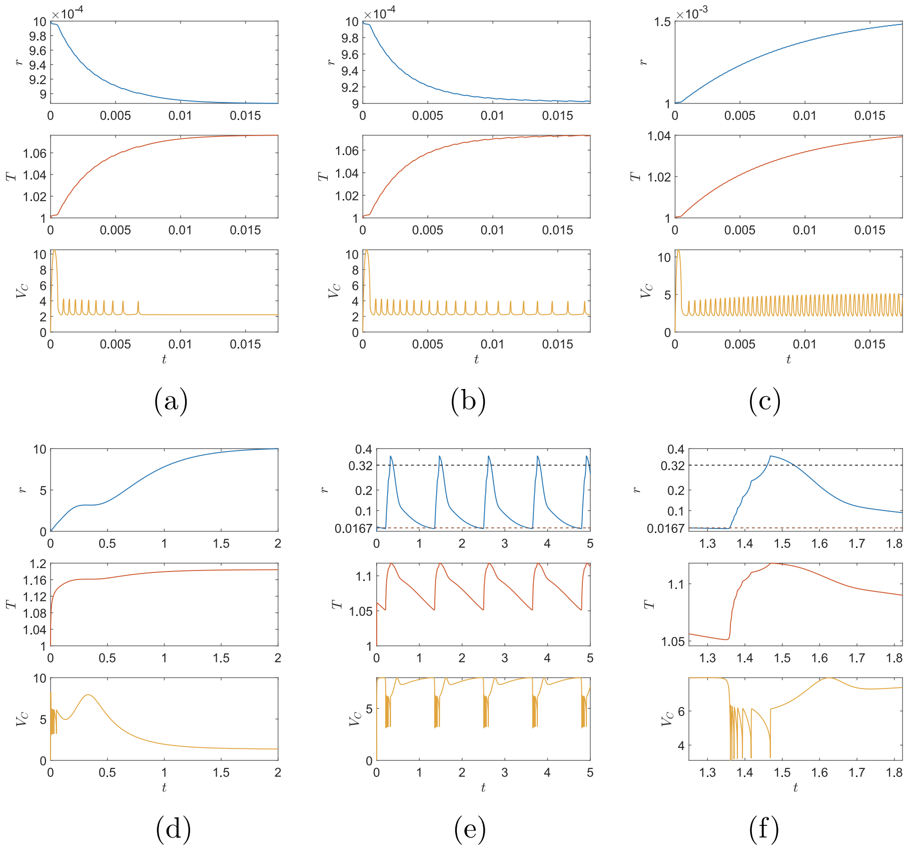

Fig. 7. Achieving complex spiking behaviors by substituting the resistor with a thermistor. (a), (b) A negative temperature coefficient thermistor of Eq. (10) and (11). (c), (d), (e), (f) A positive temperature coefficient thermistor of Eq. (12) and (13). Panel (f) is zoom-in of (e). In the simulation (a), the parameters were set as $V = 13.8564$, $\beta_1 = 1.70$, $C_1 = 5\times10^3$ and $\delta_1 = 2\times10^6$. In the simulation (b), the parameters were set as $V = 13.8564$, $\beta_1 = 1.51$, $C_1 = 5\times10^3$ and $\delta_1 = 2\times10^6$. In the simulation (c), the parameters were set as $V = 15.0111$, $\beta_2 = 10$, $C_2 = 2.5\times10^4$ and $\delta_2 = 2\times10^6$. In the simulation (d), the parameters were set as $V = 15.0111$, $\beta_2 = 50$, $C_2 = 250$ and $\delta_2 = 100$. In the simulation (e), the parameters were set as $V = 8.0829$, $\beta_2 = 50$, $C_2 = 75$ and $\delta_2 = 100$. In (e) and (f), the black dashed lines refer to r_1, and the brown dashed lines refer to r_1'. For all simulations, the background temperature T_{e1} or T_{e2} is set 1. The initial conditions are set $x = 0$, $q = 0$, and $T = 1$. (For interpretation of the references to color in this figure legend, the reader is referred to the web version of this article.)

certain resistance thresholds, say, when $r_2 < r < r_1$. Consequently, a suitable memristor (e.g., with resistance changing across r_1 and/or r_2) may be used to control the spike pattern. Here we use a negative temperature coefficient thermistor

$$r(t) = r_0 e^{\beta_1\left(\frac{1}{T}-\frac{1}{T_0}\right)} \ , \tag{10}$$

$$C_1\dot{T} = V_r(t)I_r(t) + \delta(T_{e1} - T) \ , \tag{11}$$

or positive temperature coefficient thermistor

$$r(t) = r_0 e^{\beta_2(T-T_0)} \ , \tag{12}$$

$$C_2\dot{T} = V_r(t)I_r(t) + \delta(T_{e2} - T) \ , \tag{13}$$

where T is the absolute temperature of the thermistor, β_1, β_2 are (positive) material-specific constants, C_1, C_2 are the heat capacitance, δ_1, δ_2 are the dissipation constants of the thermistor, T_{e1}, T_{e2} are the background temperatures and r_0 is the resistance at $T = T_0$. According to the above equations, in thermistors, the temperature plays the role of the internal state variable [22].

Figs. 7(a) and (b) show the results of simulations with a negative temperature coefficient thermistor defined by Eqs. (10) and (11). Approximately, the picture is as follows: The current heats the thermistor and then r starts to decrease. In Figs. 7(a), as soon as $r(t) < r_2$, the spiking terminates, and over a longer time the temperature and resistance reach equilibrium values. For Figs. 7(b), at equilibrium, the circuit spikes at a lower rate as $r(t) > r_2$ at equilibrium.

Figs. 7(c), (d), (e), and (f) show the results of simulations with a positive temperature coefficient thermistor defined by Eqs. (12) and (13). Now the heating of the thermistor increases $r(t)$, and in Figs. 7(c) the equilibrium is reached with the system spiking at a higher rate. In Fig. 7(d), the equilibrium is reached with $r(t) > r_1$, therefore, there is no spiking at longer times.

However, it is also possible to obtain more complex intermittent behaviors, switching between spiking and non-spiking. In Figs. 7(e), the increase of r is slower than in Figs. 7(d), which avoids runaway heating in the non-spiking regime. After reaching the non-spiking regime, dominated by a single sink, both voltage and current on the thermistor drop, causing it to cool and reduce its resistance, bringing the system back to the spiking regime $r < r_1$. As a consequence, the system cycles between the spiking regime and the quiescent regime. Note that the behaviors of Figs. 7(d), (e) and (f) occur only when R_0 is finite (for more details, see SI Sec. S1).

Additional results on spike generation in the memristor-leaky memcapacitor circuit can be found in SI Sec. S4 for other types of memristor.

6. Discussion and conclusion

In summary, we have proposed a leaky memcapacitor – an electromechanical crossbreed of a memcapacitor and memristor – that can generate neuromorphic spikes. Its model is based on the potential that combines linear elasticity with non-linear Lennard-Jones-like interaction between the plates at short distances, attempting to represent realistic interaction potential. Due to the presence of the nonlinear interaction, the dynamical behavior of the system in the contact region is different from the one when the plates are relatively far from each other. This helps to achieve stable spiking behavior when a constant voltage is applied.

In order to fully understand the spiking behavior, we have conducted the stability analysis in the (x, q)-space and discovered several interesting regimes characterized by different configurations of fixed points and attractors. We have shown that for some ranges of parameters, one can use a voltage pulse to switch the system from a sink to a limit cycle and vice versa. We have also found that the shape of the spike depends on the applied voltage.

An important feature of the system is that the spike frequency may adapt to the external perturbation frequency (depending on the model and excitation parameters). A rich dynamical behavior has been observed including synchronization when a small-amplitude ac signal was added to the constant driving voltage. In addition, replacing a constant external resistor with a memristor extends the variety of spike waveforms that the circuit generates. With this modification, the circuit can be tuned to mimic the behaviors of some types of biological neurons.

Experimentally, the proposed devices can be realized using membranes of suspended two-dimensional materials, including graphene [41,42]. An effective strategy is based on the use of the graphene drum capacitor [43,44]. This involves placing a layer of graphene, either single-layer [45], or multi-layer [43,44], over circular holes with typical diameters of a few micrometers [43–45][1] and suitable depths.

Wong et al. [46] used the classical theory of plates [47] to analyze graphene drums. They proposed that the drum deflection can be expressed as $d = d_0(1 - r^2/a^2)$, where d_0 represents the deflection at the center and a is the radius. The total elastic energy of the drum comprises both the bending and stretching energies, which have quadratic and quartic dependences on d_0, respectively [46]. As a result, the theory developed by us pertains to the scenario of small deflections. It is worth mentioning that the Lennard-Jones potential (the second term in Eq. (6)) is frequently used to characterize the bond between graphene and a solid surface [48]. An alternative involves the combination of an exponential term and a power term [49].

Other considerations should be taken into account. The distance between the plates should be carefully selected to allow the possibility of plate contact. The properties of the bottom electrode must be properly selected to provide a suitable contact potential and resistance. Finally, for damped dynamics (as in the model), a fluid environment may be introduced. Overall, more research and development is needed to implement the leaky memcapacitor in practice.

In general, the system introduced in this article provides a new avenue for the practical realization of neuromorphic devices based on memcapacitive and memristive effects. Our study may lead to novel energy-efficient realizations of neural dynamics with electromechanical structures, including artificial analogs of biological membranes.

CRediT authorship contribution statement

Zixi Zhang: Investigation, Software, Writing – original draft, Writing – review & editing. **Yuriy V. Pershin:** Conceptualization, Supervision, Writing – original draft, Writing – review & editing. **Ivar Martin:** Conceptualization, Supervision, Writing – original draft, Writing – review & editing.

Declaration of competing interest

The authors declare the following financial interests/personal relationships which may be considered as potential competing interests: Ivar Martin reports financial support was provided by Materials Sciences and Engineering Division, Basic Energy Sciences, Office of Science, US DOE. If there are other authors, they declare that they have no known competing financial interests or personal relationships that could have appeared to influence the work reported in this paper.

Data availability

Data will be made available on request.

Acknowledgments

I. M. acknowledges funding from the Materials Sciences and Engineering Division, Basic Energy Sciences, Office of Science, US DOE. Y. V. P. was partially supported by the National Science Foundation grant EFRI-2318139.

Appendix A. Supplementary data

Supplementary material related to this article can be found online at https://doi.org/10.1016/j.chaos.2024.114601.

References

[1] Hodgkin AL, Huxley AF. Currents carried by sodium and potassium ions through the membrane of the giant axon of Loligo. J Physiol 1952;116(4):449–72.

[2] Hodgkin AL, Huxley AF. The components of membrane conductance in the giant axon of Loligo. J Physiol 1952;116(4):473–96.

[3] Hodgkin AL, Huxley AF. The dual effect of membrane potential on sodium conductance in the giant axon of Loligo. J Physiol 1952;116(4):497–506.

[4] Hodgkin AL, Huxley AF. A quantitative description of membrane current and its application to conduction and excitation in nerve. J Physiol 1952;117(4):500–44.

[5] Hodgkin AL, Huxley AF, Katz B. Measurement of current-voltage relations in the membrane of the giant axon of Loligo. J Physiol 1952;116(4):424–48.

[6] Izhikevich EM. Dynamical systems in neuroscience: the geometry of excitability and bursting. Cambridge, Mass: MIT Press; 2007.

[7] Gerstner W, Kistler WM, Naud R, Paninski L. Neuronal dynamics: From single neurons to networks and models of cognition. Cambridge University Press; 2014.

[8] Catterall WA, Raman IM, Robinson HPC, Sejnowski TJ, Paulsen O. The Hodgkin-Huxley heritage: From channels to circuits. J Neurosci 2012;32(41):14064–73.

[9] Zhou C, Kurths J. Noise-induced synchronization and coherence resonance of a Hodgkin–Huxley model of thermally sensitive neurons. Chaos 2003;13(1):401–9.

[10] Kang Q, Huang B, Zhou M. Dynamic behavior of artificial Hodgkin–Huxley neuron model subject to additive noise. IEEE Trans Cybern 2016;46(9):2083–93.

[11] Abbott LF. Lapicque's introduction of the integrate-and-fire model neuron (1907). Brain Res Bull 1999;50(5):303–4.

[12] Fuortes MGF, Mantegazzini F. Interpretation of the repetitive firing of nerve cells. J Gen Physiol 1962;45(6):1163–79.

[13] Koch C, Segev I. Methods in neuronal modeling: from ions to networks. MIT Press; 1998.

[14] Bryant HL, Segundo JP. Spike initiation by transmembrane current: A white-noise analysis. J Physiol 1976;260(2):279–314.

[15] Izhikevich E. Simple model of spiking neurons. IEEE Trans Neural Netw 2003;14(6):1569–72.

[16] Strogatz SH. Nonlinear dynamics and chaos: with applications to physics, biology, chemistry, and engineering. CRC Press; 2018.

[17] Fortuna L, Buscarino A. Spiking neuron mathematical models: A compact overview. Bioengineering 2023;10(2). http://dx.doi.org/10.3390/bioengineering10020174.

[18] Di Ventra M, Pershin YV, Chua LO. Circuit elements with memory: Memristors, memcapacitors, and meminductors. Proc IEEE 2009;97(10):1717–24.

[19] Di Ventra M, Pershin YV. The parallel approach. Nat Phys 2013;9:200.

[20] Pershin YV, Di Ventra M. Memory effects in complex materials and nanoscale systems. Adv Phys 2011;60(2):145–227.

[21] Pershin YV, Di Ventra M. Experimental demonstration of associative memory with memristive neural networks. Neural Net 2010;23:881.

[22] Chua LO, Kang SM. Memristive devices and systems. Proc IEEE 1976;64:209–23.

[23] Chua L, Sbitnec V, Kim H. Hodgkin–Huxley axon is made of memristors. Int J Bifurcation Chaos 2012;22(03):1230011.

[24] Heimburg T. The capacitance and electromechanical couplingg of lipid membranes close to transitions: The effect of electrostriction. Biophys J 2012;103(5):918–29.

[25] Chen H, Garcia-Gonzalez D, Jérusalem A. Computational model of the mechanoelectrophysiological coupling in axons with application to neuromodulation. Phys Rev E 2019;99(3):032406.

[26] Jing H, Das S. Electric double layer electrostatics of lipid-bilayer-encapsulated nanoparticles: Toward a better understanding of protocell electrostatics. Electrophoresis 2018;39(5–6):752–9.

[27] Galassi VV, Wilke N. On the coupling between mechanical properties and electrostatics in biological membranes. Membranes 2021;11(7):478.

---

[1] There are no apparent constraints on decreasing the size of graphene drums by up to two orders of magnitude.

[28] Holland L, de Regt HW, Drukarch B. Thinking about the nerve Impulse: The prospects for the development of a comprehensive account of nerve impulse propagation. Front Cell Neurosci 2019;13:208.

[29] Martinez-Rincon J, Di Ventra M, Pershin YV. Solid-state memcapacitive system with negative and diverging capacitance. Phys Rev B 2010;81(19):195430.

[30] Martinez-Rincon J, Pershin YV. Bistable nonvolatile elastic-membrane memcapacitor exhibiting a chaotic behavior. IEEE Trans Electron Devices 2011;58(6):1809–12.

[31] Najem JS, Hasan MS, Williams RS, Weiss RJ, Rose GS, Taylor GJ, et al. Dynamical nonlinear memory capacitance in biomimetic membranes. Nature Commun 2019;10(1):3239.

[32] Liu R, Dong R, Qin S, Yan X. A new type artificial synapse based on the organic copolymer memcapacitor. Org Electron 2020;81:105680.

[33] Pershin YV, Di Ventra M. Memcapacitive neural networks. Electron Lett 2014;50(3):141–3.

[34] Scott HL, Bolmatov D, Podar PT, Liu Z, Kinnun JJ, Doughty B, et al. Evidence for long-term potentiation in phospholipid membranes. Proc Natl Acad Sci 2022;119(50):e2212195119.

[35] Demasius K-U, Kirschen A, Parkin S. Energy-efficient memcapacitor devices for neuromorphic computing. Nat Electron 2021;4(10):748–56.

[36] Ling T, Boyle KC, Zuckerman V, Flores T, Ramakrishnan C, Deisseroth K, et al. High-speed interferometric imaging reveals dynamics of neuronal deformation during the action potential. Proc Natl Acad Sci 2020;117(19):10278–85.

[37] Johnson AS, Winlow W. The soliton and the action potential – Primary elements underlying sentience. Front Physiol 2018;9:779.

[38] Appali R, van Rienen U, Heimburg T. A comparison of the Hodgkin–Huxley model and the soliton theory for the action potential in nerves. In: Advances in planar lipid bilayers and liposomes, vol. 16, Elsevier; 2012, p. 275–99.

[39] Andersen SSL, Jackson AD, Heimburg T. Towards a thermodynamic theory of nerve pulse propagation. Prog Neurobiol 2009;88(2):104–13.

[40] Heimburg T, Jackson AD. The thermodynamics of general anesthesia. Biophys J 2007;92(9):3159–65.

[41] Chen C, Hone J. Graphene nanoelectromechanical systems. Proc IEEE 2013;101(7):1766–79.

[42] Castellanos-Gomez A, Singh V, van der Zant HSJ, Steele GA. Mechanics of freely-suspended ultrathin layered materials. Ann Phys 2015;527(1–2):27–44.

[43] Davidovikj D, Scheepers PH, Van Der Zant HS, Steeneken PG. Static capacitive pressure sensing using a single graphene drum. ACS Appl Mater Interfaces 2017;9(49):43205–10.

[44] Rosłoń IE, Japaridze A, Steeneken PG, Dekker C, Alijani F. Probing nanomotion of single bacteria with graphene drums. Nature Nanotechnol 2022;17(6):637–42.

[45] Lee C, Wei X, Kysar JW, Hone J. Measurement of the elastic properties and intrinsic strength of monolayer graphene. Science 2008;321(5887):385–8.

[46] Wong C, Annamalai M, Wang Z, Palaniapan M. Characterization of nanomechanical graphene drum structures. J Micromech Microeng 2010;20(11):115029.

[47] Timoshenko S, Woinowsky-Krieger S, et al. Theory of plates and shells, vol. 2, McGraw-hill New York; 1959.

[48] Klaver T, Zhu S-E, Sluiter M, Janssen G. Molecular dynamics simulation of graphene on cu (1 0 0) and (1 1 1) surfaces. Carbon 2015;82:538–47.

[49] Reguzzoni M, Fasolino A, Molinari E, Righi MC. Potential energy surface for graphene on graphene: Ab initio derivation, analytical description, and microscopic interpretation. Phys Rev B 2012;86(24):245434.